Pressure tunes electrical resistivity by four orders of magnitude in amorphous $Ge_2Sb_2Te_5$ phase-change memory alloy

M. Xu[a], Y. Q. Cheng[a,b], L. Wang[c,d], H. W. Sheng[e], Y. Meng[f], W. G. Yang[c], X. D. Han[g], and E. Ma[a,1]

[a]Department of Materials Science and Engineering, the Johns Hopkins University, Baltimore, MD 21218; [b]Chemical and Engineering Materials Division, Oak Ridge National Laboratory, Oak Ridge, TN 37381; [c]High Pressure Synergetic Consortium, Carnegie Institution of Washington, Argonne, IL 60439; [d]State Key Laboratory of Superhard Materials, Jilin University, Changchun, 130012, China; [e]School of Physics, Astronomy and Computational Sciences, George Mason University, Fairfax, VA 22030; [f]High Pressure Collaborative Access Team, Carnegie Institution of Washington, Argonne, IL 60439; and [g]Institute of Microstructure and Property of Advanced Materials, Beijing University of Technology, Beijing 100022, China

Edited by Alexis T. Bell, University of California, Berkeley, CA, and approved March 6, 2012 (received for review November 30, 2011)

Ge-Sb-Te-based phase-change memory is one of the most promising candidates to succeed the current flash memories. The application of phase-change materials for data storage and memory devices takes advantage of the fast phase transition (on the order of nanoseconds) and the large property contrasts (e.g., several orders of magnitude difference in electrical resistivity) between the amorphous and the crystalline states. Despite the importance of Ge-Sb-Te alloys and the intense research they have received, the possible phases in the temperature–pressure diagram, as well as the corresponding structure–property correlations, remain to be systematically explored. In this study, by subjecting the amorphous $Ge_2Sb_2Te_5$ (*a*-GST) to hydrostatic-like pressure (*P*), the thermodynamic variable alternative to temperature, we are able to tune its electrical resistivity by several orders of magnitude, similar to the resistivity contrast corresponding to the usually investigated amorphous-to-crystalline (*a*-GST to rock-salt GST) transition used in current phase-change memories. In particular, the electrical resistivity drops precipitously in the $P = 0$ to 8 GPa regime. A prominent structural signature representing the underlying evolution in atomic arrangements and bonding in this pressure regime, as revealed by the ab initio molecular dynamics simulations, is the reduction of low-electron-density regions, which contributes to the narrowing of band gap and delocalization of trapped electrons. At $P > 8$ GPa, we have observed major changes of the average local structures (bond angle and coordination numbers), gradually transforming the *a*-GST into a high-density, metallic-like state. This high-pressure glass is characterized by local motifs that bear similarities to the body-centered-cubic GST (*bcc*-GST) it eventually crystallizes into at 28 GPa, and hence represents a *bcc*-type polyamorph of *a*-GST.

chalcogenide glass | electrical property | pressure effects | atomic-level structure

The emerging nonvolatile phase-change memory holds the promise for next-generation data storage (1–4). A prototypical phase-change material already used in optical discs and random-access memories is the chalcogenide $Ge_2Sb_2Te_5$ alloy [GST225, abbreviated as GST hereafter, see *Materials and Methods* for background information about the various GST phases at different temperature and pressure (5–16)]. Such applications exploit the fast phase transition and the large optical (reflectivity) or electrical (resistivity) contrast between the amorphous (*a*-GST) and the metastable crystalline rock-salt-type (*rs*-GST) polymorphs (2). As an example, upon crystallization at around 420 K from *a*-GST to *rs*-GST, the electrical resistivity decreases by at least two orders of magnitude (3–5), a hallmark that enables the memory applications of this phase-change material.

What is also interesting, as will be reported below, is that without this phase change, the *a*-GST itself can also exhibit resistivity variations covering a range as wide as four orders of magnitude, in the absence of long-range order. We uncovered this possibility for property tuning entirely in the amorphous state by applying moderate hydrostatic pressure ($P = 0$ to approximately 8 GPa, "moderate" in the context of high-pressure experiments), as this thermodynamic variable, when compared with temperature, offers a wider window for experimentation without inducing crystallization. The phase transitions and associated property changes in chalcogenides under applied pressure have been investigated before (6–12). However, most of those glasses are unable to remain amorphous at high pressures: They crystallize at $P < 10$ GPa and turn metallic-like via an abrupt drop of resistivity upon crystallization (7). A few other chalcogenide glasses (such as *a*-Se, *a*-As_2S_3, *a*-As_2Se_3) can survive higher pressures (10–30 GPa), with their resistivity decreasing continuously. But these chalcogenides are not phase-change materials, and their structural evolution with pressure has not been well understood. Therefore, the current study of the pressure-induced structure/property changes of a presumably more complicated chalcogenide glass (*a*-GST) will shed light on the high-pressure behavior of other chalcogenide glasses and may also reveal unique facets specific to the phase-change materials. In the following we will focus on the electrical resistivity (ρ) changes of *a*-GST, which drops most precipitously in the $P = 0$ to 8 GPa regime. We also demonstrate that when P is elevated to >20 GPa, the originally semiconducting *a*-GST in fact turns into a metallic-like glass.

We have also explored the local structural evolution responsible for the pronounced resistivity changes in the glass. In particular, we have identified an effective structural signature, which is different from commonly used local structural indicators (6–16) but relatively simple to quantify and yet highly indicative of the overall structural changes responsible for the drastic property excursion. We will also illustrate that the metallic-like *a*-GST state reached at high pressures is in fact a high-density polyamorph that has local structures bearing resemblance to that in the high-P crystallization product, a bcc phase (*bcc*-GST) induced by applying high pressure (approximately 28 GPa) on the glass (6, 8, 9, 11).

Results and Discussion

Fig. 1*A* shows the X-ray diffraction (XRD) intensity of *a*-GST under various pressures, in the P range before inducing crystallization into *bcc*-GST at $P > 28$ GPa (6, 8, 9, 11). We also performed ab initio molecular dynamics (AIMD) simulations, which will be used in the following to extract the P-induced local

Author contributions: M.X., Y.C., and E.M. designed research; M.X., Y.C., L.W., Y.M., and W.Y. performed research; L.W., Y.M., W.Y., and X.H. contributed new reagents/analytic tools; M.X., Y.C., H.S., and E.M. analyzed data; and M.X., Y.C., and E.M. wrote the paper.

The authors declare no conflict of interest.

This article is a PNAS Direct Submission.

[1]To whom correspondence should be addressed. E-mail: ema@jhu.edu.

See Author Summary on page 6796 (volume 109, number 18).

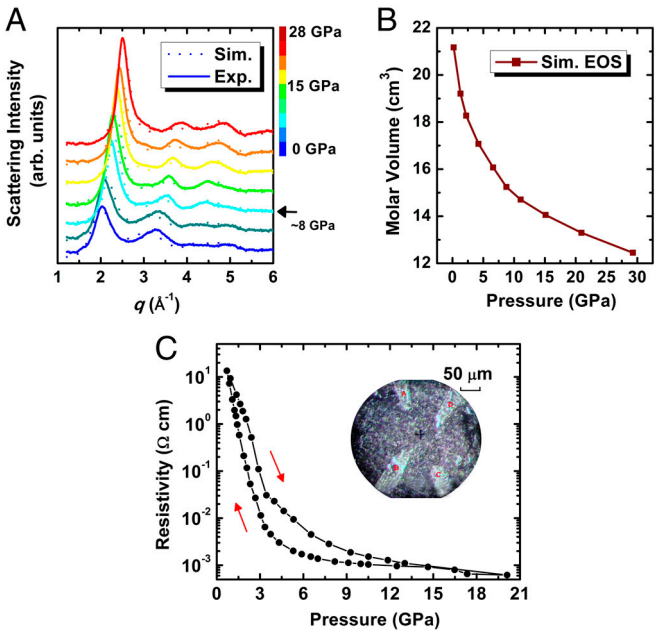

Fig. 1. (*A*) Experimentally measured (solid lines, Exp.) and simulated (dotted lines, Sim.) scattering intensities in arbitrary (arb.) units, from in situ XRD and AIMD models in the pressure range of 0–28 GPa, exhibit similar trend. The black arrow marks where 8 GPa is reached. The XRD experiment was conducted in a DAC, filled with silicone oil as the pressure-transmitting medium. (*B*) Simulated equation of states (EOS, i.e., *P-V* relation) of *a*-GST models under various pressures (up to 28 GPa, before it transforms to *bcc*-GST in experiments). (*C*) The resistivity—pressure relation of *a*-GST (the red arrows indicate the unloading and loading sequence experienced; see text). *Inset* displays an optical micrograph of the *a*-GST sample in DAC with four Pt probes.

structural evolution on the atomic level. The scattering intensities of the AIMD models at various pressures are compared in Fig. 1*A* with the experimental data. The minor disagreement between the simulations and experiments is acceptable, considering the spatiotemporal limitation of AIMD simulations (discussed in *Methods*) and the possible variants of the as-sputtered amorphous structures. The equation of states (*P-V* relation) derived from the AIMD models is plotted in Fig. 1*B*.

In the P range of 0 to 20 GPa, the electrical resistivity ρ has been measured in situ, as shown in Fig. 1*C*. The loading to high P during the first cycle ensured intimate contact between the powder particles, so the data are reported for the unloading part, together with those for the loading part of the second cycle. The ρ of the *a*-GST is approximately 20 Ωcm near ambient pressure (below 1 GPa) but drops dramatically with increasing P. Beyond $P =$ approximately 6 GPa, the decrease levels off and ρ eventually saturates at the level of approximately 10^{-3} Ωcm, exceeding the low end of the typical range for semiconductors (17). Fig. 1*C* exhibits a hysteresis loop, presumably due to some kinetic constraints and obstacles associated with the internal structural rearrangements (see below).

An inevitable residual pressure exists in the diamond anvil cell at the starting and final points of the pressure cycle, but by extrapolating the curves to $P = 0$ GPa the ρ of *a*-GST at ambient pressure can be estimated. The extrapolation suggests a value around 10^2–10^3 Ωcm, consistent with previous measurements (18, 19). More loading–unloading cycles extending to higher P produced similar ρ-P loops. These observations confirm the intimate contact between sample powders and the probes.

Pressure Compresses the Low-Electron-Density (LED) Regions in *a*-GST to Induce High Electrical Conductivity. We first focus on the lower P regime (0 to approximately 8 GPa), in which the electrical resistivity (ρ) change in *a*-GST is the most dramatic. The decrease of ρ by approximately four orders of magnitude is comparable to the potential range achievable by thermal-annealing-induced phase transitions and in fact more pronounced than that in the particular *a*-GST to *rs*-GST phase transition used in memory devices (compare Fig. 1*C* with the change of ρ as a function of annealing temperature, for example, the reported curve in ref. 3 and ref. 19).

An understanding of this P-induced precipitous ρ drop from the evolution of the underlying glass structure is of course highly important before this phenomenon can be used for applications or for guiding searches of other high-contrast memory materials. In general terms, pressure increases the mass density of the glass, and barring a phase transition, pressure-induced conductivity rise for semiconductors is often associated with the broadening and eventual overlap of the valence and conduction bands (20, 21), due to the shortening and rotation of bonds (changes in bond lengths and bond angles). To assess changes in the atomic configurations and relevant structural features (in terms of local coordination), our AIMD model configurations have been analyzed. Plotted in Fig. 2 are the partial pair correlation functions (PCFs, Fig. 2*A*), the bond-angle distribution (Fig. 2*B*), and the coordination numbers (CN_{ELF}, Fig. 2*C*) as determined based on the electron localization function (ELF) approach (13). Apparently, none of these characteristic structural parameters change significantly within the $P = 0$ to 8 GPa range (the changes at higher pressures will be analyzed in the next section). For example, the Ge-Te and Sb-Te bond lengths, which can be obtained from the first peaks in the respective PCF, remain largely unchanged. Even the Te-Te pair distance, and the bond-angle distribution (Fig. 2*B*), are observed to have experienced only minor changes in this pressure range.

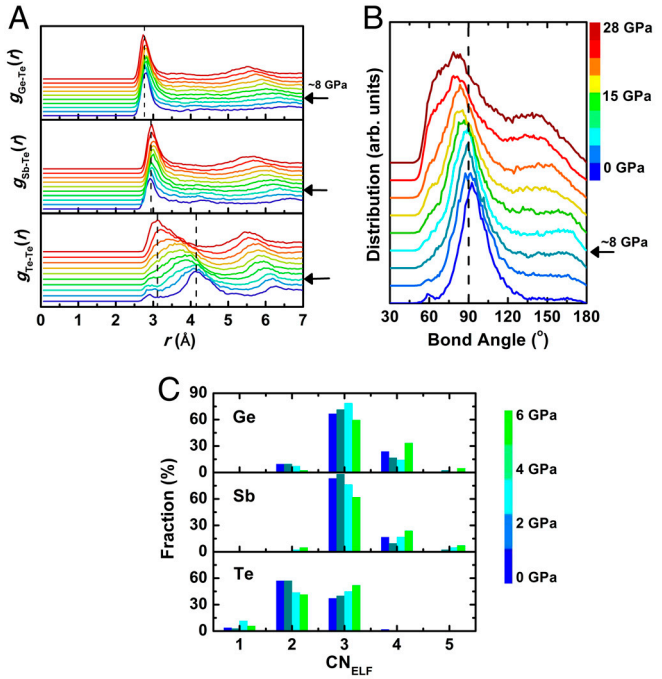

Fig. 2. Structural data extracted from the molecular dynamics models in the 0 to 28 GPa pressure regime. (*A*) Partial PCFs of Ge-Te, Sb-Te, and Te-Te. The dashed line marks the first peak at approximately 2.8/3.0 Å for the Ge-Te/Sb-Te bond lengths, and the initial/finial distance of approximately 4.2/3.1 Å for Te-Te pairs. The black arrows indicate the pressure around 8 GPa, where the structural transition is evolving from the first stage (the fast compression of LED regions) to the second stage (prominent increase of CN and decrease of bond angle) (*B*) The bond-angle distribution. The dashed line marks the 90° peak position expected for perfect octahedral coordination. (*C*) The CNs based on ELFs threshold (CN_{ELF}) surrounding each species in the low-pressure regime.

We note here that the CNs by ELF criterion only count the covalently bonded neighbors with a sufficient degree of electron localization in between. This is different from the distance cutoff method, which determines CNs solely by interatomic distances. The advantages of the ELF criterion have been discussed before (3, 13). The minor change of CN_{ELF} again suggests that the average local order and bonding in *a*-GST have not changed a great deal in the $P = 0$ to 8 GPa regime.

As such, in terms of the structural origin it is quite challenging to provide a quantitative explanation to the large ρ variations observed. The changes in the normally used structural parameters are rather small and difficult to quantify and monitor, as displayed in Fig. 2. In the following, we set out to identify an effective structural indicator to reflect/summarize the gradually changing local chemical environments, rather than dwelling on the subtle details of the complicated local structure that often involve ambiguity or arbitrary cutoffs.

To this end, we notice that intrinsically the *a*-GST at ambient pressure possesses a relatively loose structure with the presence of a significant fraction of LED regions. These regions have been previously characterized as voids/cavities by geometric criteria and proposed to be an important feature in the structure of *a*-GST (22, 23). They are analogous to the vacancies in *rs*-GST, the role of which in facilitating phase transition has been discussed by several authors (8, 10, 24). Here we examine, from the charge density perspective, the LED regions in amorphous state and their effects on the electrical resistivity. The compression-induced volume reduction of these LED regions at increasing P can be the primary reason for the density increase in this amorphous material, correlating with the rapid ρ drop.

Different from geometric tessellation that can isolate cavity-like voids from the networking atoms (22, 25), here we identify LED regions, which can be as small as atomic scale, by mapping out volumes that have electron charge density lower than a critical level. The LED regions defined as such can be visualized, as in Fig. 3, to observe the distribution of (percolated) LED regions in space. Specifically, we employed the normalized electron density (D^e_{norm}), which is the absolute electron density observed at any given location in the ab initio model, normalized by the average valence electron density of the whole system. This is necessary for a meaningful comparison of *a*-GST under different pressure, with different mass/atomic density, as plotted in Fig. 3*A*. The LED regions are those enclosed by the isosurface of D^e_{norm} at a threshold value. To determine this threshold, we used a "standard": The *rs*-GST is a defect-ridden crystal known to contain 10 at.% vacancies (or 20% on the Ge/Sb sublattice sites) (14, 26–28). In this case, we determine the D^e_{norm} threshold to be the level that results in a total vacant region amounting to 10% of the entire crystal volume (Fig. 3*B*). The same threshold is then applied to *a*-GST (dashed line in Fig. 3*A*). The LED regions (corresponding to the left-hand side of the dashed line) determined this way can thus be reasonably designated as "vacant" or "vacancy-like," and their fraction can be compared among different systems (at different pressures).

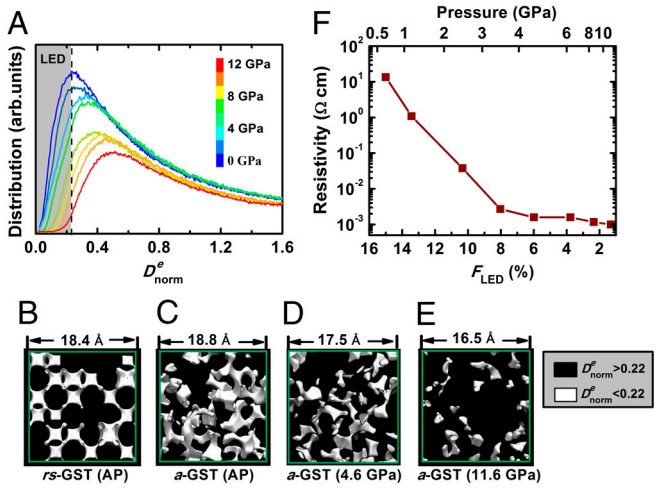

Fig. 3. (*A*) The distribution of D^e_{norm} (the absolute electron density normalized by the average electron density) in *a*-GST under various pressures. The threshold (the dashed line) to separate the vacant area is set to be 0.22, at which the volume fraction of vacancy in *rs*-GST is 10%; see the *rs*-GST reference in *B*. (*C*)–(*E*) Visualization of LED regions (The light areas with $D^e_{\text{norm}} < 0.22$) at different *P*. (*F*) The fraction of LED regions decreases rapidly with increasing pressure in the *P* < approximately 8 GPa regime, correlating with the fast resistivity reduction.

The LED regions in *a*-GST concentrate to form vacancy-like or void-like entities of various sizes (see scale markers in Fig. 3), randomly distributed inside the glass. With increasing pressure, we clearly observe a marked decrease of their volume fraction (F_{LED}) in the system, as shown in Fig. 3 *C*–*E*. At ambient pressure, it is known that *a*-GST is approximately 6.5% less dense than the *rs*-GST (29), and F_{LED} starts out at approximately 16% in our *a*-GST (6% more than that in the calculated *rs*-GST). F_{LED} turns out to be a strong function of pressure, as the electron charge density redistributes and the local motifs rearrange to arrive at different contents of the LED regions, reaching a much lower level of approximately 4% at $P = 6$ GPa.

To recap, in situ experiments have revealed that moderate pressures (0–8 GPa) on *a*-GST can reduce the electrical resistivity (ρ) of *a*-GST (Fig. 1*C*) by orders of magnitude, not possible in dense glasses such as metallic glasses (30), and to the extent similar to what is achieved via temperature-induced crystallization of *a*-GST (a first-order phase transition to *rs*-GST). Interestingly, in this pressure regime where the ρ changes most precipitously (Fig. 3), the changes in local order are neither pronounced nor easily quantifiable. Instead, the concurrent decrease in the volume fraction of the LED regions (F_{LED}) is rapid and highly noticeable, suggesting a strong correlation of the latter with ρ. This correlation, when explicitly plotted as in Fig. 3*F*, is obvious.

This correlation prompts us to take the F_{LED} as a useful indicator to effectively reflect the overall changes in local structures, in explaining the large resistivity contrast. In fact, LED regions themselves are a meaningful structural feature that is worthy of studying, complementary to the tracking of atoms, their configurations, and bonding details. Here we note that whereas the average structure, as reflected by the PCFs in Fig. 2*A*, does not change much, the local structures around the LED regions may have experienced more changes. In other words, the structural change that governs the resistivity behavior is believed to be inhomogeneous and concentrated locally around the LED regions. Because F_{LED} can be unambiguously defined and changes continuously, the reduction of LED volumes serves as a simple and yet revealing signature to summarize/represent the evolving atomic-level structure, the latter being the ultimate structural origin of property variations in glass.

To substantiate the important role of F_{LED} on ρ in this P regime, we consider an amorphous semiconductor with localized states in its band gap and the Fermi energy (E_F) lying in the middle of the gap (see the energy band diagram for *a*-GST in refs. 3 and 4). The electronic transport can be understood as having two possible mechanisms: (1) the trap-limited Poole–Frenkel conduction, for which the resistivity follows (4, 31)

$$\rho^{-1} \propto \exp\left(-\frac{E_C - E_F - \Delta\phi_{\text{field}}}{k_B T}\right), \qquad [1]$$

where E_C is the mobility edge in the conduction band. In this mechanism, localized electrons are thermally activated to become extended electrons, contributing to the electrical conduction (32, 33). In addition, some extended electrons can be

trapped by the unoccupied localized states near E_C, and the release of these trapped electrons to the extended state, or the thermally assisted hopping to a nearby unoccupied localized state, has a field dependence, giving rise to a field-dependent term, $\Delta\phi_{\text{field}}$ (this term is estimated to be orders of magnitude smaller than E_C-E_F in our experiment). (2) the variable-range hopping (34), which refers to phonon-assisted tunneling of electrons from one localized state to another near the Fermi level. The logarithm of the electrical conductivity governed by this mechanism has a $T^{-1/4}$ dependence on temperature, whereas that due to Poole-Frenkel conduction is expected to scale with T^{-1} (see **1** above). Based on the different temperature dependence, previous studies have concluded that variable-range hopping does not play a significant role in *a*-GST (4, 31, 35). Therefore, the electrical conductivity of *a*-GST should scale exponentially with E_C-E_F. The dependence of the latter on pressure, as explained in the following, holds the key to understanding the precipitous ρ drop (by several orders of magnitude). First of all, the band gap (the "optical gap" between the bottom of the conduction band and the top of the valence band) of *a*-GST is expected to decrease with increasing pressure. An obvious reason that can lead to a reduced band gap is that the fewer the (originally abundant) LED regions, the stronger the interactions between the local structural motifs or "clusters," leading to broadened energy bands (35, 36). Our ab initio energy band calculation indeed supports this proposition, as indicated by the density of states (DOS) under different *P* plotted in Fig. 4*A*. The band gap obtained may not be accurate in absolute values (37), but the trend is clear for the broadening of the valence band and the shrinking of the band gap.

Note that to confirm the controlling role of LED regions, we also preformed ab initio calculations on another set of *a*-GST models, in which the atomic density changes and the same range of pressure (0 to 8 GPa) are generated solely by scaling the bond lengths, without structural relaxation that diminishes the LED regions in the original models. These unrelaxed models did not exhibit major band gap changes in the same *P* regime. This result can be understood by considering the two factors that affect the band gap: (1) the compressed bond length increases the bonding–antibonding splitting (in contrast to the relaxed model, where this splitting is not changed due to near-constant bond length); (2)

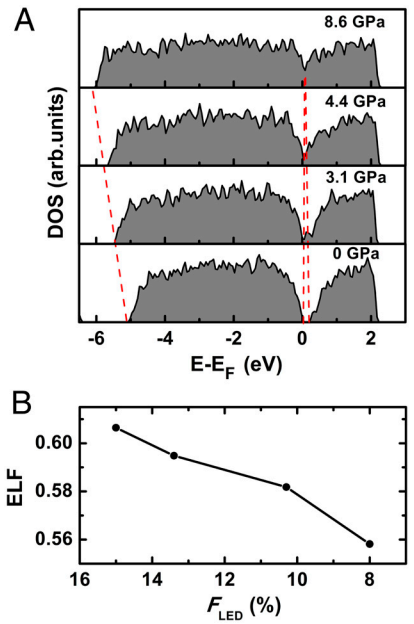

Fig. 4. (*A*) The electron DOS of *a*-GST in the low pressure regime. The red dashed lines in *A* show the broadening of the valence band and narrowing of the band gap. (*B*) The average value of the ELFs in the bonding areas, decreasing with the volume reduction of LED regions.

The reduction of LED volumes (though far less significant as the relaxed models) enhances the interactions between local clusters, expanding the band width. The two contributions largely cancel out, leading to little change in the band gap (35).

Second, in addition to calculating the change in band gap, we use ELF to provide evidence that some localized electrons in *a*-GST become more delocalized with diminishing LED regions. The average ELF calculated for the bonding electrons is shown in Fig. 4*B*. Electrons with ELF toward 1 are more localized than those with ELF toward lower values (38). Fig. 4*B* suggests a trend that some originally trapped electrons become less localized at high *P*, signifying a shift of the mobility edges and narrowing of the band tails (34). This, taken together with the reduced band gap, indicates that the mobility gap is effectively reduced. E_C-E_F is thus expected to decrease, resulting in the exponential increase of the charge carrier density and hence of the conductivity. This is a different approach in tuning the electrical resistivity compared to the annealing-induced disorder–order transition (17).

An important implication of our discussion is that the LED regions may also play an important role in the resistivity contrast between *a*-GST and *rs*-GST (which we use in today's devices), given that *a*-GST has 6% more LED fraction than *rs*-GST. We have shown that by tuning the volume fraction of often-localized LED regions in the glassy state itself (or vacancies in the crystal), large resistivity contrast can result. This is a desirable feature for applications in memory devices (18, 19). Also, GST in real devices is likely to work under certain level of pressure [e.g., several hundred MPa either from the confinement or due to the density change upon phase transition (29)]; understanding the *P*-sensitivity of ρ and its structural origin would therefore be of practical importance. The use of either one of the two thermodynamic variables, *P* or *T* (e.g., heat treatment to crystallize *a*-GST into *rs*-GST), when reducing the LED/vacancies to the same level, may produce similar ρ. Of course, different from *P*, the thermal crystallization of *a*-GST will include other types of structural changes, e.g., the bonding nature (the resonant bonding and the long-range order mentioned earlier upon phase change to *rs*-GST) (39–41). Nevertheless, Fig. 3 suggest that shrinking LED regions should play an important role in inducing, or contributing to, the large resistivity contrast relative to the as-prepared *a*-GST. Indeed, heat treatment can further reduce the vacancy content in the *rs*-GST crystal when it is transformed to the stable phase trigonal-GST (*t*-GST). This *t*-GST also has local structures similar to *rs*-GST (42), but its resistivity is even lower (i.e., becoming a degenerate semiconductor) (17).

High Pressure Leads to a Unique Polyamorph. We now proceed to discuss the discoveries at $P > 8$ GPa. Recent studies of *a*-GST showed that at ambient pressure, although there is a small fraction of tetrahedrally bonded Ge (30% of Ge), most (approximately 93% out of all) atoms are in the center of defective octahedral sites (15), and the bond angles tend to be around 90 °. These features suggest that in terms of the most general description, the local structure of *a*-GST bears some resemblance to that of *rs*-GST, which has a distorted rock-salt structure due to vacancies and Peierls distortion (14). We thus name the *a*-GST at ambient pressure *rs*-type *a*-GST (it, however, should be noted that there are also salient differences in the structure/bonding details of *a*-GST and *rs*-GST, as explained in the ref. 3). The scattering intensity, CN_{DIS} [coordination numbers (CNs) based on the distance cutoff] and bond-angle distribution of the *rs*-type *a*-GST at ambient pressure are shown in Fig. 5 *A*–*C*, in comparison with the crystalline *rs*-GST. Here the CN_{DIS} is the number of geometrical neighbors based on a uniform distance cutoff (3.2 Å in this study), used here in lieu of the CN_{ELF} (CNs based on the threshold of the ELFs) to allow a comparison with the high-*P* structures reported in Fig. 5 *D*–*F* (at high pressures CN_{ELF} cannot be determined, see discussion in *Methods*). The CN_{DIS} of *rs*-type *a*-GST at

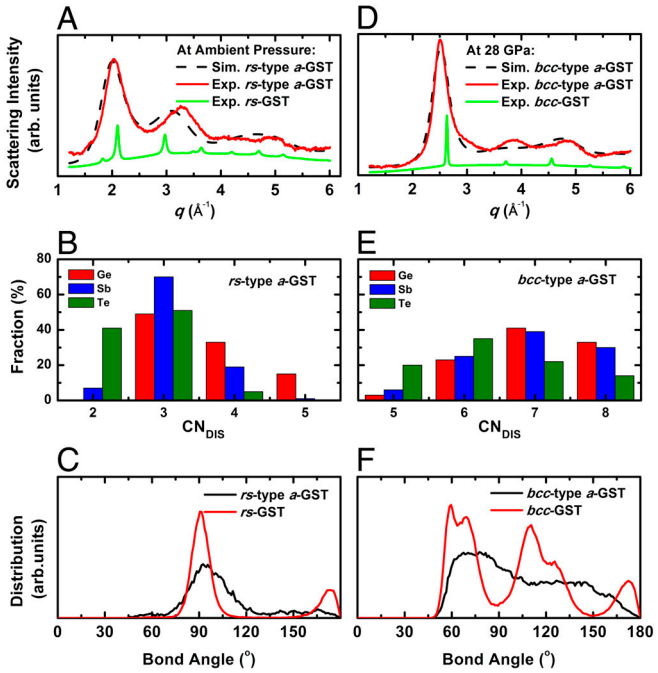

Fig. 5. Structural parameters, including (*A*) experimental and simulated scattering intensity, (*B*) simulated CNs, and (*C*) bond-angle distributions, of *rs*-type *a*-GST and *rs*-GST at ambient pressure. The same three parameters for *bcc*-type *a*-GST and *bcc*-GST at high pressure ($P = 28$ GPa) are shown in *D*, *E*, and *F*, respectively. Here the CN is determined using the distance cutoff method; see explanation in *Methods*.

ambient pressure shows similar results as the CN_{ELF} obtained from ELF threshold, with threefold Ge/Sb and Te in both twofold and threefold forms. In comparison, in the *rs*-GST Ge/Sb are mostly sixfold and Te four- and fivefold, enabled by the resonant bonds that are highly symmetric (40). Such a difference is expected, because the glass is devoid of the long-range order in *rs*-GST and the atomic clusters are separated by LED regions (39). As we discussed above (e.g., Fig. 2), the *rs*-type *a*-GST persists through the $P = 0$ to 8 GPa range, whereas the compression of LED regions dominates.

The structural evolution away from *rs*-type *a*-GST starts around $P = 8$ GPa. As seen in Fig. 2, the bond angle begins to be compressed at approximately 8 GPa, with gradual shortening of the Te-Te bond distance. Now the atoms tend to be surrounded by more geometric neighbors. This trend becomes more obvious after 15 GPa, when the LED regions are squeezed down to a very low content ($F_{LED} < 1\%$). Fig. 5 *D*–*F* shows the structural parameters derived for the *a*-GST compressed to 28 GPa (right before it crystallizes into *bcc*-GST). Now the X-ray scattering intensity profile exhibits resemblance to that of the *bcc*-GST, a solid solution with randomly distributed species, crystallized from *a*-GST at high pressures (6); see Fig. 5*D*. Meanwhile, the packing efficiency becomes higher, and the CN_{DIS} tending toward 8 is much larger than *rs*-type *a*-GST (compare Fig. 5*E* with Fig. 5*B*). Moreover, the bond angles now have a wide distribution (Fig. 5*F*,) starting from approximately 55°, which is a typical angle in bcc lattices. This high-*P* *a*-GST is therefore better recognized as *bcc*-type *a*-GST, such that it is identified as a unique form of *a*-GST clearly distinguishable from the *rs*-type *a*-GST in Fig. 5 *A*–*C*. One can envision that it is the large numbers of bcc-like local motifs that join hands to obtain the long-range order upon crystallization under further compression.

The presence of a high-density form of *a*-GST (see density information in Fig. 1*B*) was in fact predicted by Sun et al. in their recent simulations (43) for a high pressure around 30 GPa. The simulation suggested that the bond angles shift toward 60° and CNs approach 8, all different from the *rs*-type *a*-GST. Sun et al. named this high-*P* *a*-GST configuration *t*-amorphous GST, as it was assumed to resemble the crystalline (trigonal) phase stable at ambient conditions. However, there has been no experimental confirmation of this prediction so far. Our high-*P* work did find such a high-density state, but it is believed that this high-*P* *a*-GST can be better described as of bcc type, because it bears close local structural resemblance to the bcc crystallization product and can be viewed as the precursor of the latter.

We now spell out the entire structural evolution of the *a*-GST under pressure, combining the information in Fig. 2 and Fig. 5. The first peaks of Ge-Te and Sb-Te distances (Fig. 2*A*), which are located around 2.8 Å and 3.0 Å, respectively, come from the bond length in the covalent glass. With increasing pressure, these bond lengths are largely unaltered up to 28 GPa before crystallization into *bcc*-GST (9, 11). This is consistent with the notion that the covalent bonds are rather stiff. In comparison, other structural parameters such as LED regions and bond angles are more prone to changes under pressure. Take the evolution of Te-Te distance (Fig. 2*A*) as an example. At ambient pressure, the Te atoms in *rs*-type *a*-GST are located in the hypotenuse positions of an isosceles-like right triangle, which are separated by a distance of about 4.2 Å [a small fraction of Te-Te neighbors ("wrong bonds") gives rise to the small peak around 2.8 Å]. This right-angled scenario of the local structure, which is the signature of the *rs*-type *a*-GST, is sustainable up to 8 GPa, until the LED regions are compressed to occupy only a small fraction of the total volume. The Te-Te distance becomes shorter when *P* is larger than 8 GPa, indicating ongoing compression of the Te-Ge(Sb)-Te bond angles, ending up with a peak of 3.2 Å at 28 GPa. In this medium-to-high-pressure regime (8 to 28 GPa), electron charge redistributes to such an extent that the LED regions no longer survive above 15 GPa, such that the increasing packing efficiency is almost solely due to the reduction of bond angles. The overall *rs*-type to *bcc*-type transition appears to be gradual, without abrupt changes in the structure (and ρ in Fig. 1), in contrast to some Si/SiO_2 glasses or liquids (44, 45).

Fig. 6 summarizes the descriptions above. In the low-pressure regime, the LED regions in *rs*-type *a*-GST are compressed down first without obvious changes in the bond length and angle. The *rs*-type *a*-GST is largely retained up to 8 GPa, beyond which the bond angle starts to change significantly. The transition from the *rs*-type *a*-GST to the *bcc*-type *a*-GST involves both the rotation of the bonds and the formation of new bonds (such as Te-Te nearest-neighbor bonds). The local structure of the final *bcc*-type *a*-GST glass resembles the (110) plane of the bcc lattice, and bcc-like embryos in *a*-GST appear around 20 GPa and are enhanced with the increase of pressure, facilitating subsequent transformation into the bcc crystal at approximately 28 GPa. In comparison, in Fig. 6 we have also sketched the structural evolution by compressing the crystalline *rs*-GST, which was proposed by Caravati et al. (10). In this case, the compression of the Ge(Sb)-Te bonds destabilizes the *rs*-GST, when the atoms flip into the preexisting neighboring vacancy regions in the lattice, leading to the collapse of the crystal into the *a*-GST.

In the $P > 8$ GPa regime, the electrical resistivity decrease has leveled off, almost reaching a plateau in Fig. 1*C*. Apparently, with the band gap closing upon the reduction of the volume of the LED regions in the $P = 0$–8 GPa regime, the density of charge carriers is remarkably increased. Further compression (>8 GPa) leads to the overlap of the valence band and the conduction band, and the semiconductor evolves toward metallic-like, with nearly constant density of charge carriers afterwards. The variation in ρ thus becomes moderate, despite the obvious local structural changes described above for the high-*P* regime. The pressure-induced semiconducting-to-metallic transition in *a*-GST is similar to the insulating-to-metallic transition (MIT) observed in *rs*-GST and *t*-GST (17). But instead of moving the E_F into the valence

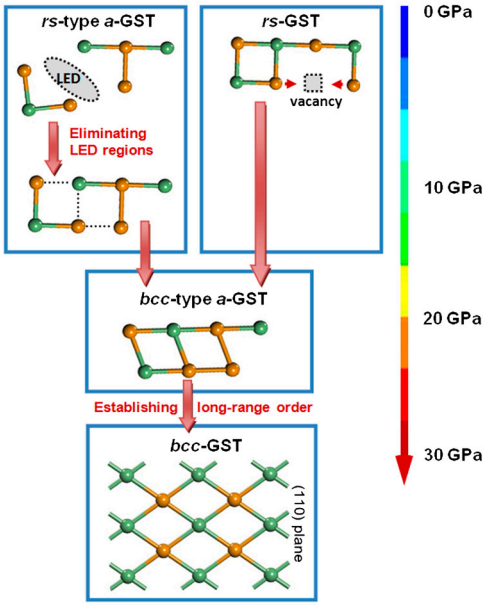

Fig. 6. Local structure evolution upon compression (0–30 GPa), initially from *rs*-type *a*-GST or *rs*-GST (10), to *bcc*-type *a*-GST, and eventually to *bcc*-GST. In the lower pressure regime (0–8 GPa), the LED regions in *rs*-type *a*-GST are removed first, without significant changes to the local motifs. After most of the LED regions are removed, the bond angles start to decrease and the glass transforms into the high-density, metallic-like *bcc*-type *a*-GST before crystallization into *bcc*-GST. In comparison, pressure on the *rs*-GST crystal displaces the atoms around the existing vacancies, amorphizing the latter into the *bcc*-type *a*-GST at 20 GPa (8, 10). The green balls stand for Te atoms, and orange ones Ge/Sb.

band (below the mobility edge) by ordering the crystals in the MIT transition, our *a*-GST glass experiences evident band gap closing during the compression. The final metallic-like products, the ordered *t*-GST in ref. 17 and *bcc*-type *a*-GST in our study, have similar electrical resistivity around 10^{-3} Ωcm, close to the upper bound of the metallic regime (34).

Conclusion

In summary, we have performed in situ XRD and electrical resistivity measurement on as-sputtered *a*-GST under (nominally) hydrostatic pressure, and discovered two distinct regimes, each with unique property and structural features, before the glass crystallizes into *bcc*-GST.

First, a precipitous resistivity drop with increasing pressure is discovered in the $P <$ approximately 8 GPa regime. The large (approximately four orders of magnitude) span in resistivity in the amorphous phase without crystallization, suggests ample room and variability in the electrical property of *a*-GST that are potentially useful for memory applications. We have probed into the structural origin of this property contrast. Our AIMD simulations showed that in this pressure range, changes in average bonding and structure (bond length, bond strength, bond angle, and CNs as determined from ELFs) are rather subtle and thus difficult to correlate with. However, interestingly, our analysis uncovered a prominent indicator that reveals pronounced evolution of structure and electron distribution: the volume fraction of vacancy-like entities, characterized as LED regions in *a*-GST. The structural evolution in this pressure regime is in fact characterized by the fast compression of LED regions. The important role of this factor is perhaps not surprising, considering the relatively loose structure of the *a*-GST, which increases its density by as much as approximately 7% upon crystallization to *c*-GST (which still contains as much as 10% vacancies). We have observed a strong correlation: The pronounced decrease of F_{LED} (volume fraction of LED regions) is concurrent with the fast decreasing resistivity. The volume reduction of the LED regions may enhance the chemical interaction between the local atomic clusters and broaden the energy bands, thus narrowing the band gap and increasing the number of charge carriers. Meanwhile, the amorphous system becomes more locally ordered, and some originally trapped electrons are hence delocalized, which moves the mobility edge and contributes to the electrical conduction. Therefore, we believe that the compressing LED regions serve as an important structural signature for the pressure-induced large resistivity change in *a*-GST and as such best embody the overall underlying changes in bonding and atomic-level structures.

Second, by further increasing the pressure beyond 8 GPa, the local structure of the *rs*-type *a*-GST starts to switch toward a different type, becoming evident at $P > 15$ GPa when the LED regions diminish. A prominent increase of CN and decrease of bond angle then takes over to dominate the structural evolution in this pressure regime. The packing efficiency is primarily increased by the reducing bond angles under compression, leading consequently to bcc-like motifs that characterize the high-*P*, high-density glass. At approximately 28 GPa the glass eventually turns into *bcc*-type *a*-GST, a unique polyamorph that we propose to reflect its resemblance to the high-pressure bcc crystallization product. The phase evolution sequence observed under pressure supports and clarifies the prediction given by computer calculations. The covalent *bcc*-type *a*-GST glass becomes metallic-like, and its electrical resistivity saturates in the approximately 10^{-3} Ωcm range, similar to other chalcogenide glasses at approximately 30 GPa and close to the level of metals.

Materials and Methods

Background Information About the GST Phases. The metastable crystalline phase *rs*-GST is composed of two sets of sublattices: The anion sites are fully occupied by Te atoms and the cation sites are occupied by 40% Ge, 40% Sb, and 20% vacancies (14). This crystalline lattice is found to be severely distorted and the local structures contain "defective octahedra." Similar structures are found for the local motifs of *a*-GST, which is *rs*-type at ambient pressure but contains some tetrahedrally coordinated Ge (13, 15, 16).

By heating the *rs*-GST to approximately 600 K, some of the vacancies are removed (42) and it transforms into the trigonal GST (*t*-GST), along with a property transition from semiconductor to metal that can be explained by the order–disorder transition (17). Using pressure as a trigger, the *t*-GST becomes an orthorhombic-like crystal (*o*-GST, with lower vacancy concentration) at approximately 17 GPa and is eventually pressed into a body-centered-cubic solid solution (*bcc*-GST, without vacancies) at approximately 30 GPa (9, 12). The final bcc product could also be obtained by compressing *a*-GST or *rs*-GST to approximately 30 GPa (without observing the *o*-GST along the way) (6, 11). The pressure-induced property change for the GST polymorphs and the responsible structural origin, however, have not been systematically studied.

In Situ XRD Experiment Under High Pressure. The *a*-GST samples were prepared by sputtering $Ge_2Sb_2Te_5$ onto an amorphous silica substrate. The as-sputtered *a*-GST powders were immersed in the silicone oil (as pressure transmitting medium) and was compressed hydrostatically in diamond anvil cell (DAC). In situ XRD was used to monitor the structural change. The high-pressure experiments were carried out at the 16ID-B station of the High-Pressure Collaborative Access Team, Advanced Photon Source, Argonne National Laboratory. The DAC was used to generate pressure (*P*) in the range of 0–33 GPa. The pressure was measured with the ruby fluorescence method (46). The increment and decrement of each pressure step was 3–5 GPa, and the samples were allowed to relax for 20 min at each pressure point. The monochromatic synchrotron X-ray with the wavelength of 0.36229 Å enabled us to obtain reliable diffraction patterns up to a scattering vector of approximately 6.0 $Å^{-1}$ in the presence of the DAC. The scattering background was measured in the sample-free area at each pressure step.

In Situ Electrical Resistivity (ρ) Measurement Under High Pressure. The *a*-GST powders from the same sputtered films as in the XRD experiment were used for electrical resistivity measurement. Another DAC with anvil culets of 400 μm was used for generating high pressure, which was also monitored by using the ruby fluorescence method. A T301 stainless steel preindented at approximately 23 GPa was used as a gasket and a hole with a diameter

of 300 μm was drilled in the center of the indentation. Insulating amorphous boron powder was used to fill the hole and cover the gasket to minimize the influence of the steel on our ρ measurement. A smaller hole of 150 μm was drilled in the center of the amorphous boron after preloading (approximately 18 GPa) and filled with *a*-GST powder removed from the substrate. Four Pt foil probes (2 μm thick, marked as A, B, C, and D) were implanted (Fig. 1*C*, *Inset*). The sample and the Pt probes were preloaded to 3 GPa to remove the spaces between powders for full contact of the sample with the probes. Pressure transmitting medium was not used during ρ measurement because it would permeate into the spacing between powder pieces and interfere with their intimate contact upon pressuring. Considering *a*-GST is a material with good malleability, the powders are expected to act as the pressure transmitting medium themselves to generate hydrostatic-like pressures.

The pressure (*P*) was changed in steps of 0.5 to 1.0 GPa and the system was allowed to equilibrate for 30 min at each pressure point. A 1 mA electrical current (resulting in very small current density) was injected between probes A and C, and the resistance (R_1) between B and D was recorded. Another resistance (R_2) measurement was then made by switching to probes B and C. The van der Pauw equation was used to determine ρ (47):

$$\exp\left(-\frac{\pi L R_1}{\rho}\right) + \exp\left(-\frac{\pi L R_2}{\rho}\right) = 1, \qquad [2]$$

where *L* is the thickness of the sample (20 μm). The plastic change in *L* under pressure is negligible because the gasket had been prehardened at 23 GPa. The cross-sectional area in which the electrical current was injected was estimated to be several hundred μm^2, much larger than the one used between the electrode tips (nm^2 scale) (48), thus the injected 1 mA current would not be sufficient to induce structural changes including the *a*-*c* transition. The applied pressure while measuring the electrical resistivity was limited to 22 GPa so as to prevent the possible crystallization and keep the GST entirely in the amorphous state.

AIMD Simulations. The AIMD simulations were performed by the Vienna ab initio simulation package (VASP) code (49) and the projector augmented-wave method (50, 51) with the generalized gradient approximations. A box with 189 atoms was quenched from liquid at 3,000 K to room temperature (RT) at 20 K/ps. The temperature was controlled using the Nose-thermostat (52). The mass density during the quenching was fixed at the estimated experimental value of *a*-GST at RT (approximately 5.8 g/cm^3, which is 6% lower than the mass density of *rs*-GST) (14, 29, 39) and the zero-pressure density can be obtained by relaxing the quenched glass. After the system was equilibrated at RT for 3,000 time steps (3 fs/step), volume reductions were applied to the amorphous system, 1% strain for each step and 50 steps in total, to further obtain different configurations at various pressures. This isotropic stepwise volume reduction in AIMD simulations to mimic the experimental hydrostatic compression has been adopted in recent AIMD studies on pressure-induced structural changes (6, 10, 43, 53). The spatiotemporal limitation of AIMD simulation is a major issue that needs to be considered when interpreting the results and comparing with experiments. In our case, the different degree of structural relaxation undergone in the simulated samples and in the laboratory ones, as well as the statistical fluctuations associated with the small box size (189 atoms), may possibly lead to different structures. The differences are, however, not expected to be significant, particularly for the general trend of structural evolution. For example, we used both athermal and AIMD (at 300 K) simulations to study the pressure-induced structural changes, and the results are statistically identical. A second sample under loading–unloading cycles yields similar equation of states.

Two Approaches to Determine the CNs. We have used two methods to calculate the CN. The first method evaluates the CN_{ELF}, based on the threshold of ELF, which was generated by VASP in the grid of $60 \times 60 \times 60$ matrix. To obtain the ELF profile, the two relevant atoms are connected with a tube (radius = 0.36 Å), which is evenly divided into 21 sections. ELF data points included in each section are then averaged, and the 21 averaged ELF values profile the bond between the two atoms. The strength of the covalent bonds is reflected by the ELF values in the middle area that are averaged so that we have a quantitative evaluation of the bonding strength. The threshold is set to be ELF = 0.58, below which the bonds are believed to be too weak to be included in the CN. The CN_{ELF} reflects the numbers of chemically bonded neighbors. However, this method is not applicable at high pressures. Here the bond angle is compressed down and the "tubes" to calculate the ELF profile overlap. Also, free electrons prevail in the high-pressure regime and are intertwined with the localized electrons. All these factors undermine the accuracy in determining the CN_{ELF} at high pressures.

The second method evaluates the CN_{DIS} based on distance cutoff, which is chosen to be slightly larger than the bond length. In our calculation, the distance cutoff is set to be 3.2 Å. Physically, the CN_{DIS} represents the number of geometric neighbors and no electronic property is considered. As such, CN_{DIS} is less accurate than CN_{ELF} in identifying the truly bonded neighbors in covalent glasses. However, it can be readily applied in the whole pressure range (especially when the bonding turns metallic-like at high pressures), such that it is adopted in Fig. 5 for the purpose of comparing the low-*P* and high-*P* structures. An example of the difference between CN_{ELF} and CN_{DIS} is the different fractions of fourfold Ge and twofold Te (Fig. 2*C* and Fig 5*B*) because CN_{DIS} fails to identify the dative bonds between Ge and Te (13, 54).

ACKNOWLEDGMENTS. The authors are indebted to Prof. Ju Li for discussions about the mechanisms of electrical conduction in glasses. This work is supported by Materials Sciences and Engineering Division, Office of Basic Energy Sciences (BES), Department of Energy (DOE, DE-FG02-09ER46056 for J.H.U.), by Scientific User Facilities Division, BES, DOE (for Y.Q.C. at Oak Ridge National Laboratory), by the Office of Naval Research (09PR08570-00/1054998 for H.W.S.), EFree (an Energy Frontier Research Center funded by the DOE-BES-DE-SC0001057 for L.W. and W.G.Y.), and the Chinese National Basic Research Program (2007CB935400 for X.D.H.). The XRD experiments were conducted at Sector 16IDB of the High-Pressure Collaborative Access Team (funded by DOE-BES, DOE National Nuclear Security Administration, National Science Foundation, and the W.M. Keck Foundation), Advanced Photon Source (DOE-BES, DE-AC02-06CH11357), Argonne National Laboratory.

1. Ovshinsky SR (1968) Reversible electrical switching phenomena in disordered structures. *Phys Rev Lett* 21:1450–1453.
2. Wuttig M, Yamada N (2007) Phase-change materials for rewriteable data storage. *Nat Mater* 6:824–832.
3. Lencer D, Salinga M, Wuttig M (2011) Design rules for phase-change materials in data storage applications. *Adv Mater* 23:2030–2058.
4. Raoux S, Welnic W, Ielmini D (2010) Phase change materials and their application to nonvolatile memories. *Chem Rev* 110:240–267.
5. Friedrich I, Weidenhof V, Njoroge W, Franz P, Wuttig M (2000) Structural transformations of $Ge_2Sb_2Te_5$ films studied by electrical resistance measurements. *J Appl Phys* 87:4130–4134.
6. Xu M, et al. (2010) Pressure-induced crystallization of amorphous $Ge_2Sb_2Te_5$. *J Appl Phys* 108:083519.
7. Parthasarathy G, Gopal E (1985) Effect of high pressure on chalcogenide glasses. *Bulletin of Materials Science* 7:271–302.
8. Kolobov AV, et al. (2006) Pressure-induced site-selective disordering of $Ge_2Sb_2Te_5$: A new insight into phase-change optical recording. *Phys Rev Lett* 97:035701.
9. Krbal M, et al. (2009) Initial structure memory of pressure-induced changes in the phase-change memory alloy $Ge_2Sb_2Te_5$. *Phys Rev Lett* 103:115502.
10. Caravati S, Bernasconi M, Kuhne TD, Krack M, Parrinello M (2009) Unravelling the mechanism of pressure induced amorphization of phase change materials. *Phys Rev Lett* 102:205502.
11. Cheng YQ, et al. (2009) A body-centered-cubic polymorph of the $Ge_2Sb_2Te_5$ phase change alloy. *Appl Phys Lett* 95:131904.
12. Kalkan B, Sen S, Clark SM (2011) Nature of phase transitions in crystalline and amorphous GeTe-Sb_2Te_3 phase change materials. *J Chem Phys* 135:124510.
13. Xu M, Cheng YQ, Sheng HW, Ma E (2009) Nature of atomic bonding and atomic structure in the phase-change $Ge_2Sb_2Te_5$ glass. *Phys Rev Lett* 103:195502.
14. Matsunaga T, Yamada N, Kubota Y (2004) Structures of stable and metastable $Ge_2Sb_2Te_5$, an intermetallic compound in GeTe-Sb_2Te_3 pseudobinary systems. *Acta Crystallogr Sect B-Struct Sci* 60:685–691.
15. Caravati S, Bernasconi M, Kuhne TD, Krack M, Parrinello M (2007) Coexistence of tetrahedral- and octahedral-like sites in amorphous phase change materials. *Appl Phys Lett* 91:171906.
16. Mazzarello R, Caravati S, Angioletti-Uberti S, Bernasconi M, Parrinello M (2010) Signature of tetrahedral Ge in the Raman spectrum of amorphous phase-change materials. *Phys Rev Lett* 104:085503.
17. Siegrist T, et al. (2011) Disorder-induced localization in crystalline phase-change materials. *Nat Mater* 10:202–208.
18. Privitera S, Rimini E, Zonca R (2004) Amorphous-to-crystal transition of nitrogen- and oxygen-doped $Ge_2Sb_2Te_5$ films studied by in situ resistance measurements. *Appl Phys Lett* 85:3044–3046.
19. Lankhorst MHR, Ketelaars BWSMM, Wolters RAM (2005) Low-cost and nanoscale non-volatile memory concept for future silicon chips. *Nat Mater* 4:347–352.
20. Ma YM, et al. (2009) Transparent dense sodium. *Nature* 458:182–185.
21. Arai K, et al. (1973) Pressure effects on electrical conduction in glasses. *J Non Cryst Solids* 13:131–139.
22. Akola J, Jones RO (2008) Binary alloys of Ge and Te: Order, voids, and the eutectic composition. *Phys Rev Lett* 100:205502.
23. Sun ZM, Zhou J, Blomqvist A, Johansson B, Ahuja R (2009) Formation of large voids in the amorphous phase-change memory $Ge_2Sb_2Te_5$ alloy. *Phys Rev Lett* 102:075504.

24. Wuttig M, et al. (2007) The role of vacancies and local distortions in the design of new phase-change materials. *Nat Mater* 6:122–127.
25. Akola J, Jones RO (2007) Structural phase transitions on the nanoscale: The crucial pattern in the phase-change materials $Ge_2Sb_2Te_5$ and GeTe. *Phys Rev B* 76:235201.
26. Liu XQ, et al. (2011) New structural picture of the $Ge_2Sb_2Te_5$ phase-change alloy. *Phys Rev Lett* 106:025501.
27. Kolobov AV, et al. (2004) Understanding the phase-change mechanism of rewritable optical media. *Nat Mater* 3:703–708.
28. Da Silva JLF, Walsh A, Lee HL (2008) Insights into the structure of the stable and metastable $(GeTe)_m(Sb_2Te_3)_n$ compounds. *Phys Rev B* 78:224111.
29. Pedersen TPL, et al. (2001) Mechanical stresses upon crystallization in phase change materials. *Appl Phys Lett* 79:3597–3599.
30. Zeng QS, et al. (2010) Properties of polyamorphous $Ce_{75}Al_{25}$ metallic glasses. *Phys Rev B* 82:054111.
31. Ielmini D, Zhang YG (2007) Evidence for trap-limited transport in the subthreshold conduction regime of chalcogenide glasses. *Appl Phys Lett* 90:192102.
32. Frenkel J (1938) On pre-breakdown phenomena in insulators and electronic semiconductors. *Phys Rev* 54:647–648.
33. Hill RM (1971) Poole–Frenkel conduction in amorphous solids. *Philos Mag* 23:59–86.
34. Mott NF (1969) Conduction in non-crystalline materials. 3. Localized states in a pseudogap and near extremities of conduction and valence bands. *Philos Mag* 19:835–852.
35. Zallen R (1998) *The Physics of Amorphous Solids* (Wiley-VCH, New York), Classics Library Edition.
36. Im J, et al. (2010) Effects of pressure on atomic and electronic structure and crystallization dynamics of amorphous $Ge_2Sb_2Te_5$. *Phys Rev B* 81:245211.
37. Hafner J, Wolverton C, Ceder G (2006) Toward computational materials design: The impact of density functional theory on materials research. *MRS Bull* 31:659–665.
38. Becke AD, Edgecombe KE (1990) A simple measure of electron localization in atomic and molecular-systems. *J Chem Phys* 92:5397–5403.
39. Hegedus J, Elliott SR (2008) Microscopic origin of the fast crystallization ability of Ge-Sb-Te phase-change memory materials. *Nat Mater* 7:399–405.
40. Shportko K, et al. (2008) Resonant bonding in crystalline phase-change materials. *Nat Mater* 7:653–658.
41. Matsunaga T, et al. (2011) From local structure to nanosecond recrystallization dynamics in AgInSbTe phase-change materials. *Nat Mater* 10:129–134.
42. Sun ZM, Zhou J, Ahuja R (2006) Structure of phase change materials for data storage. *Phys Rev Lett* 96:055507.
43. Sun ZM, et al. (2011) Pressure-induced reversible amorphization and an amorphous-amorphous transition in $Ge_2Sb_2Te_5$ phase-change memory material. *Proc Natl Acad Sci USA* 108:10410–10414.
44. McMillan PF, Wilson M, Daisenberger D, Machon D (2005) A density-driven phase transition between semiconducting and metallic polyamorphs of silicon. *Nat Mater* 4:680–684.
45. Sen S, Gaudio S, Aitken BG, Lesher CE (2006) Observation of a pressure-induced first-order polyamorphic transition in a chalcogenide glass at ambient temperature. *Phys Rev Lett* 97:025504.
46. Mao HK, Xu J, Bell PM (1986) Calibration of the ruby pressure gauge to 800-Kbar under quasi-hydrostatic conditions. *J Geophys Res* 91:4673–4676.
47. van der Pauw LJ (1958) A method of measuring specific resistivity and Hall effect of discs of arbitrary shape. *Philips Res Rep* 13:1–9.
48. Ielmini D, Lacaita AL, Mantegazza D (2007) Recovery and drift dynamics of resistance and threshold voltages in phase-change memories. *IEEE Trans Electron Devices* 54:308–315.
49. Kresse G, Furthmuller J (1996) Efficiency of ab-initio total energy calculations for metals and semiconductors using a plane-wave basis set. *Comput Mater Sci* 6:15–50.
50. Kresse G, Joubert D (1999) From ultrasoft pseudopotentials to the projector augmented-wave method. *Phys Rev B* 59:1758–1775.
51. Blochl PE (1994) Projector Augmented-Wave Method. *Phys Rev B* 50(24):17953–17979.
52. Allen MP, Tidesley DJ (1989) *Computer Simulation of Liquids* (Clarendon, Oxford).
53. Sheng HW, et al. (2007) Polyamorphism in a metallic glass. *Nat Mater* 6:192–197.
54. Krbal M, et al. (2011) Intrinsic complexity of the melt-quenched amorphous $Ge_2Sb_2Te_5$ memory alloy. *Phys Rev B* 83:054203.